"Cookie": A Satellite Concept for GNSS Remote Sensing Constellations

Manuel Martín-Neira, *Senior Member, IEEE*, Weiqiang Li, Ana Andrés-Beivide, and Xabier Ballesteros-Sels

***Abstract*—This paper presents a concept, "Cookie," for a satellite particularly suited for dense spatial sampling by future Global Navigation Satellite Systems (GNSS) remote sensing constellations. Solely based on the reception of the direct and reflected signals transmitted by the GNSS, the satellite can provide observations of the Earth useful for a wide range of scientific and operational applications. The Cookie is capable of receiving direct and reflected signals, in both right- and left-hand circular polarizations, from any of the GNSS systems, and from virtually any arrival direction in both the upper and lower field-of-view hemispheres, i.e., providing nearly full 4π spherical coverage toward any navigation satellite not eclipsed by the Earth. The on-board remote sensing payload produces interferometric observables, e.g., the auto- and cross-correlation of several adequate combinations of the received signals. The interferometric processing is general, the same, and transparent, with respect to any of the signals transmitted by the current or planned GNSS systems. The instrument can implement any other suitable processing schemes too. Such payload can provide, in parallel, accurate GNSS Radio-Occultation (GNSS-RO) observations of the atmosphere and forward and backward GNSS Reflectometry (GNSS-R) measurements from the Earth surface. Several Cookies can be piled up inside the fairing of a rocket minimizing the launch cost of a constellation. A constellation of three Cookies has been simulated and its sampling performance characterized. The key concepts of the Cookie payload could be demonstrated through ESA's GNSS Reflectometry, Radio-Occultation, and Scatterometry experiment on board the International Space Station (GEROS-ISS).**

***Index Terms*—Global navigation satellite systems reflectometry (GNSS-R), GNSS radio-occultation (GNSS-RO), GNSS reflectometry, radio-occultation, and scatterometry on-board the International Space Station (GEROS-ISS).**

I. Introduction

As early as in the 1980s and in parallel to the development of GPS and GLONASS, the first scientific applications using the navigation signals of the newly-born Global Navigation Satellite Systems (GNSS) were conceived. The first one, in the field of concern to us, i.e., Earth remote sensing from space, was atmospheric sounding through radio-occultation (GNSS-RO), proposed by the Jet Propulsion Laboratory in 1988 [1], [2], based on experience gained from several planetary missions [3], [4]. A few years later, in 1993, came reflectometry (GNSS-R), put forward by the European Space Agency (ESA) for mesoscale ocean altimetry as an alternative concept to a constellation of pulse-limited nadir looking radar altimeters [5], [6]. GNSS-R was further extended to cover several other remote sensing applications [7], like wind over ocean [8], [9], sea ice monitoring [10], [11], ice sheet sounding [12], soil moisture [13], and biomass [14].

The first mission dedicated to test GPS radio-occultation was the GPS Meteorological mission (GPS/MET), launched in 1995 [15], but it took some years before the potential of the technique was recognized. Following GPS/MET, radio-occultation experiments were performed by missions which had a different main objective though, such as the Challenging Mini-satellite Payload (CHAMP) [16] and the Satélite de Aplicaciones Científicas-C (SAC-C) [17] in 2000, and the Gravity Recovery and Climate Experiment (GRACE-A) [18] in 2002, to name the very early ones. Currently there is a good number of spaceborne missions and constellations carrying (or planned to carry in the near future) dedicated GNSS-RO payloads, for example, the FORMOSAT/COSMIC constellation [19], the EUMETSAT-ESA's meteorological METOP series or the EU-ESA's Global Monitoring for Environmental Security Sentinel satellites. GNSS-RO is therefore a consolidated technique that is being used routinely in operational meteorology.

Although the evidence of reflected signals had been reported in the measurements of some of the previously mentioned radio-occultation missions [20], the most relevant and pioneering experience regarding GNSS-R from space came in 2003 from the Disaster Monitoring Constellation 1 satellite (UK-DMC 1) [21]. Based on the successful recording of reflected signals by UK-DMC 1, sometimes even beyond expectations, a second satellite, TechDemoSat-1 (TDS-1), has been recently launched (July 8, 2014), with a more capable GNSS-R receiver [22] on board. An evolution of such receiver will be further embarked on each of the eight microsatellites of NASA's Cyclone Global Navigation Satellite System (CyGNSS) in late 2016 [23]. Being the first pathfinder mission using the GNSS-R technique for a practical application, CyGNSS constitutes a real milestone. Other GNSS-R space missions have been or are under study elsewhere too, but without flight approval yet [24], [25].

The landscape of GNSS remote sensing space missions described above presents a well-marked differentiation between those dedicated to radio-occultation from those devoted to reflectometry. There have been mission concepts, though, to perform both types of observations, as the AMORE constellation [26], and, at a lower level, also receiver designs conceived for

Manuscript received June 12, 2015; revised May 31, 2016; accepted June 17, 2016. Date of publication August 17, 2016; date of current version October 14, 2016. *(Corresponding author: Manuel Martín-Neira.)*

M. Martín-Neira is with the European Space Agency, Noordwijk 2200-AG, The Netherlands (e-mail: manuel.martin-neira@esa.int).

W. Li is a postdoc at the Institute of Space Sciences (ICE-IEEC/CSIC), Barcelona 08193, Spain (e-mail: weiqiang.li.buaa@gmail.com).

A. Andrés-Beivide is with the EADS CASA Espacio, Madrid 28022, Spain (e-mail: Ana.Andres@astrium.eads.net).

X. Ballesteros-Sels is with the Space Division, Mier Communicaciones, La Garriga 08530, Spain (e-mail: xballesteros@mier.es).

Color versions of one or more of the figures in this paper are available online at http://ieeexplore.ieee.org.

Digital Object Identifier 10.1109/JSTARS.2016.2585620

the same dual purpose [27], [28]. But even in these hybrid missions and receivers, occultation and reflected signals are received through different antenna sets.

In contrast to any known mission concept, this paper presents a satellite and payload concept particularly devised to perform remote sensing with GNSS signals at its maximum extent possible, i.e., by efficiently combining reflectometry and radio-occultation.

II. "Cookie" Satellite

The original concept of passive reflectometry and interferometry system (PARIS) with GNSS signals in [5] describes a system in which the direct signal is, after being shifted in time and Doppler properly, cross correlated against the reflected signal collected by a beamforming antenna. This idea, referred to as *interferometric* GNSS-R, or GNSS-Ri, was only tested experimentally from a bridge in July 2010 [29], and, more importantly, from an aircraft over the Baltic Sea in November 2011 [30]. These two experiments demonstrated the better performance achievable with the interferometric approach over the use of clean replicas of the navigation codes, or GNSS-Rc, the technique which had been used exclusively (or with minor variants) up to that moment. Interferometric GNSS-Ri attains its advantage when wide bandwidth encrypted codes are present in some of the navigations links, and when applied from space, as only in this case, the geometry enables discrimination across different GNSS satellites through the antenna beam, the time delay and the Doppler frequency shift. Alternative techniques to GNSS-Ri, achieving comparable performance, have been proposed elsewhere, for example, in [34] and [35], which could also be incorporated into the satellite concept here proposed.

The interferometric technique was further elaborated in the PARIS In-orbit Demonstration mission concept (PARIS IoD) [24] for which the signal-to-noise ratio (SNR) was derived in detail, and a swapping technique proposed, associated to a particular antenna and front-end architecture, to remove instrumental errors. PARIS IoD was a mini-satellite aiming at demonstrating GNSS-R from space, and can be considered the starting configuration in the inception of the "Cookie" satellite.

The real push to transform PARIS IoD into a "Cookie" comes when the German Research Centre for Geoscience (GFZ) proposed to ESA the "GNSS REflectometry, Radio-Occultation and Scatterometry on-board the International Space Station" experiment, or GEROS-ISS in short [25], [39], [40]. GEROS-ISS represents a truly qualitative jump over past missions in that the proposing scientific team defines a multi-application experiment, comprising the observation of surface-reflected as well as atmosphere-refracted GNSS signals in a variety of geometries. The conventional approach of using different antennas, receivers, and techniques, for radio-occultation and reflectometry, is abandoned in GEROS-ISS, where instead, one antenna package and one processing technique are proposed for all applications [31].

The "Cookie" satellite, or simply, the *Cookie*, is obtained when the GEROS-ISS payload is conceptually detached from the International Space Station and arranged into a free-flying satellite. The platform functionalities provided by the ISS are then incorporated along a perimetric structural extension of the central antenna array package. Of the different processing techniques, the GNSS-Ri interferometric technique is the one proposed for the Cookie, which can in addition incorporate other approaches based on clean code replicas or semi-codeless techniques, to improve performance in specific applications, or to better counteract radio-frequency effects from radar services sharing the navigation frequency bands. A novelty of the Cookie over the prior art is the realization of radio-occultation using the same GNSS-Ri interferometric approach as for reflectometry, a concept described first in [32]. An artist view of the Cookie is shown in Fig. 1, from which the reader will realize the origin of its name.

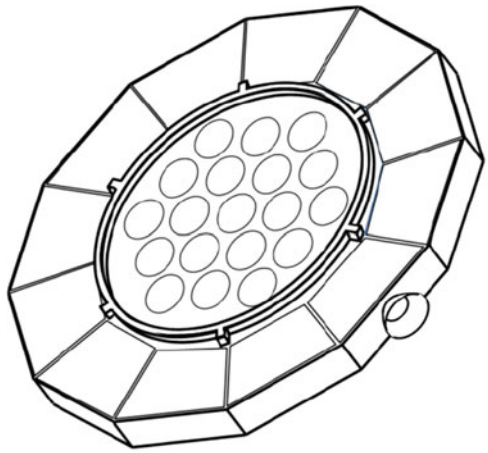

Fig. 1. "Cookie" satellite concept: the center is dedicated to the double face beam-forming antenna array, the outer area providing space for the payload electronics, platform subsystems, and solar cells; the middle ring constitutes the main structure and hosts the hold down and release mechanisms. The version depicted is provided with a thruster. The diameter of this particular Cookie is about 1.8 m, and its height around 20 cm.

The Cookie includes all key functionalities specified for the GEROS-ISS payload in [31], comprising reflectometry (forward and backward scattering) as well as radio-occultation, in at least two of the radio-navigation bands (GPS L1 and L5, GLONASS L1OC and L3OC/L5OC, GALILEO E1 and E5, BeiDou B1 and B2, QZSS L1, L5, etc.) in fully polarimetric mode, to enhance land and other atmospheric applications.

In addition, a number of Cookie satellites can be conveniently stacked one on top of another inside the fairing of a rocket, for the launch of a constellation of Cookies, in a very similar way as the four CLUSTER satellites were accommodated inside the Arianne V rocket or the six FORMOSAT-3/COSMIC-1 satellites aboard the Minotaur-I.

Depending on whether the Cookies have propulsion or not, and whether it is chemical or electrical, a different strategy for their release and orbital deployment into their final orbital position can be followed. The Cookie flies nominally Earth-pointed, with its perpendicular axis pointing toward the Earth. In this way its two antennas can access a large number of both reflected and refracted signals.

In the following sections, the main characteristics of the Cookie are explained in further detail.

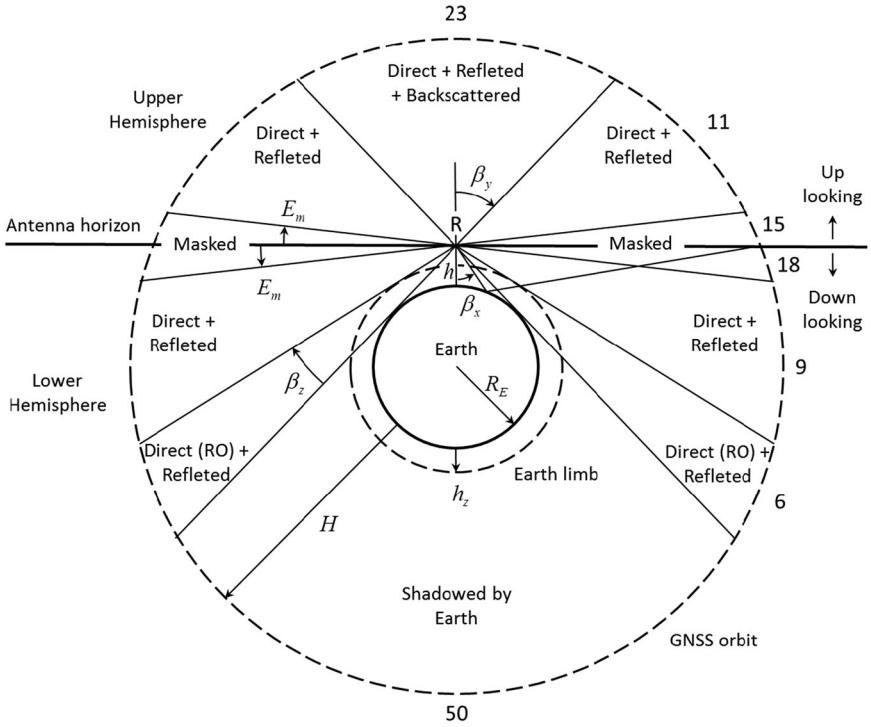

Fig. 2. GNSS signals accessibility by an Earth-pointed Cookie. The legend in each sector indicates the type of observations possible with GNSS satellites in that sector. For example, GNSS satellites in the top sector generate direct, reflected and backscattered signals; those in its adjacent sections provide only direct and reflected signals, etc. The numbers next to each sector indicate the average number of GNSS satellites in that sector for the $h = 800$ km case of Table I.

III. Combining GNSSRO and GNSS-R in a Cookie

Following the establishment of the GNSS interferometric technique for radio-occultation in [32], it is possible to describe how a Cookie can perform GNSS radio-occultation and reflectometry in an efficiently combined way. Assume the Cookie R flying at some Low Earth Orbit (LEO) altitude *h*, with its perpendicular axis pointed normal to the Earth surface, as depicted in Fig. 2.

In the central part of the Cookie, the up-looking and down-looking antennas have their respective front hemispheres free of any obstacles which could produce blockage or multipath, and have thus clear view to receive incoming signals from any direction within them.

A. Number of Beams

Let M_x and M_y be the average number of visible GNSS satellites in the upper and lower hemispheres respectively. All M_x and M_y GNSS satellites can be used for reflectometry, as every one of them has a corresponding reflection point on the Earth surface, assumed as a spherical mirror. In addition, the subset M_{y1} (of the M_y satellites) seen through the Earth limb (see nadir angle range $\beta_y < \beta < \beta_y + \beta_z$ in Fig. 2) provide radio-occultation events. Other reflection points of interest are the backscatter points, i.e., the projections of the receiving point *R* onto the surface of the Earth along the paths of the direct signals. Only the subset M_{x1} (of the M_x GNSS satellites) lying in between the tangents to the Earth from *R* (zenith angle range $\beta < \beta_y$) do generate such projection points on the Earth surface.

To measure all reflected signals, on average, the up-looking antenna must be able to generate and steer M_x beams in any direction in the upper hemisphere. Similarly, the down-looking antenna must have $M_x + M_{x1}$ steerable beams for the M_x and M_{x1} forward and backward reflection points, respectively, corresponding to the GNSS satellites in the upper hemisphere. In addition, the down-looking antenna must have, in general, other $2M_y$ beams for the direct and reflected signals of the M_y GNSS satellites in the lower hemisphere, which include M_{y1} beams for the rising and setting GNSS satellites in the Earth limb. So, in total, the down-looking beamformer must have $M_x + M_{x1} + 2M_y$ beams.

To consider some reduction in the number of beams may be practical at this point. On one hand, near the antenna horizon, the directivity of the beams drops substantially due to the element pattern roll off, and an elevation mask angle E_m can always be defined below which no observations are attempted. On the other hand, the elevation angle subtended by the Earth limb (defined here by the lowest $h_z = 250$ km of the atmosphere) when seen from an LEO is no more than some $\beta_z = 7°$ (see Fig. 2), smaller than the beamwidth of a typical Cookie antenna when steered toward the limb (of the order of 10° for a 1–2-m antenna diameter) so that both the direct and reflected signals of a radio-occultation event can be received through the same beam. Taking into account these two reductions, the number of up- and down-looking beams, B_x and B_y, respectively, becomes

$$B_x = M_x - M_{\mathrm{xm}} \quad (1)$$

$$B_y = B_x + M_{x1} + M_{y1} + 2(M_y - M_{\mathrm{ym}} - M_{y1}) \quad (2)$$

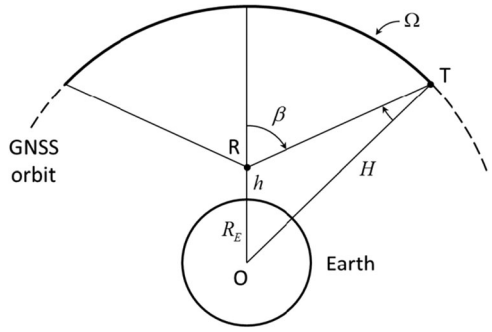

Fig. 3. Supporting geometry in the computation of the number of beams.

where $M_{\rm xm}$ and $M_{\rm ym}$ are the GNSS satellites at lower elevation than the mask angle E_m in the upper and lower hemispheres, respectively. It is apparent, from (1) and (2), that a Cookie must have more down-looking than up-looking beams to gather all the possible mentioned observations.

Using the geometry in Fig. 3, the solid angle of a cone with vertex at *R* and semiangle β is given by

$$\Omega = 2\pi(1 - \cos(\beta - T)) \tag{3}$$

with *T* being the angle with vertex at the transmitter

$$T = \arcsin\left(\frac{R_E + h}{R_E + H}\sin\beta\right) \tag{4}$$

and therefore, assuming a total of *M* GNSS satellites uniformly distributed over a sphere of radius *H*, the following estimations can be derived:

1) Average number of GNSS satellites in upper hemisphere

$$M_x = \frac{1}{2}\frac{H - h}{R_E + H}M. \tag{5}$$

2) Part of the M_x satellites inside upper hemisphere mask

$$\begin{aligned} M_{\rm xm} &= M_x - \frac{1}{2}\left(1 - \sin(E_m + T_m)\right)M \\ T_m &= \arcsin\left(\frac{R_E + h}{R_E + H}\cos E_m\right). \end{aligned} \tag{6}$$

3) Part of the M_x satellites which can generate backscattering

$$\begin{aligned} M_{x1} &= \frac{1}{2}\left(1 - \cos(\beta_y - T_y)\right)M \\ \beta_y &= \arcsin\frac{R_E}{R_E + h} \quad T_y = \arcsin\frac{R_E}{R_E + H}. \end{aligned} \tag{7}$$

4) Average number of GNSS satellites in lower hemisphere

$$M_y = \frac{1}{2}\left(1 + \cos(\beta_y + T_y)\right)M - M_x. \tag{8}$$

5) Part of the M_y satellites inside lower hemisphere mask

$$M_{\rm ym} = \frac{1}{2}\left(1 + \sin(E_m - T_m)\right)M - M_x. \tag{9}$$

TABLE I
(A) NUMBER OF UP-LOOKING ($B_{\rm x}$) AND DOWN-LOOKING ($B_{\rm y}$) BEAMS A COOKIE SHOULD HAVE, ON AVERAGE, TO OBSERVE FORWARD AND BACKWARD REFLECTIONS, AS WELL AS RADIO-OCCULTATIONS, FROM FOUR GNSS CONSTELLATIONS, ASSUMED OF 33 SATELLITES EACH, I.E., $M = 132$ IN (5)–(10), UNIFORMLY SPACED AT 20 920-KM ALTITUDE (AVERAGE HEIGHT OF GPS, GLONASS, BEIDOU, AND GALILEO), (B) NUMBER OF GNSS SATELLITES FOR (5)–(10) AND (C) ANGLES—IN DEGREES—CORRESPONDING TO (5)–(10)

h	$B_{\rm x}$	$B_{\rm y}$
400	34	66
800	33	81
1300	32	93

(a)

h	$M_{\rm x}$	$M_{\rm x1}$	$M_{\rm xm}$	$M_{\rm y}$	$M_{\rm y1}$	$M_{\rm ym}$
400	50	30	15	24	9	18
800	49	23	15	33	6	18
1300	47	17	15	42	4	18

(b)

h	$T_{\rm m}$	$\beta_{\rm y}$	$T_{\rm y}$	$\beta_{\rm z}$	$T_{\rm z}$	$E_{\rm m}$
400	13.9	70.2	13.5	7.7	14.0	15
800	14.7	62.7	13.5	4.7	14.0	15
1300	15.7	56.1	13.5	3.5	14.0	15

(c)

6) Part of the M_y satellites which are setting or rising, i.e., whose signal traverses the Earth atmosphere

$$\begin{aligned} M_{y1} &= M_x + M_y - \frac{1}{2}\left(1 + \cos(\beta_y + \beta_z + T_z)\right)M \\ \beta_z &= \arcsin\frac{R_E + h_z}{R_E + h} - \beta_y \quad T_z = \arcsin\frac{R_E + h_z}{R_E + H}. \end{aligned} \tag{10}$$

Based on (5)–(10), Table I presents the number of up-looking and down-looking beams for three different values of orbital height *h*, which are representative of the International Space Station and several Earth Observation missions, such as 400 km (GEROS-ISS), 800 km (ERS-1/2, ENVISAT, Cryosat, METOP, Saral/AltiKa, Sentinel-3, and SWOT), 1300 km (Topex/Poseidon and JASON series), as well as all intermediate values used to derive them. From Table I(a) it is clear that the number of up-looking beams is quite insensitive to the orbital height of the Cookie, slightly decreasing for higher altitudes. On the contrary, the number of down-looking beams, which is about twice the number of up-looking beams at 400-km altitude, increases sensibly with orbital height, reaching nearly three

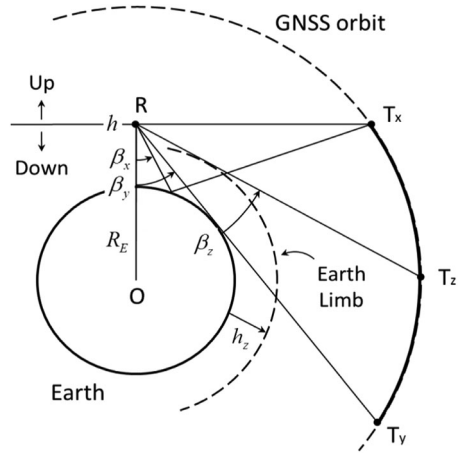

Fig. 4. Geometry supporting the discussion on down-looking beams polarization and types of observations.

times as many at a height of 1300 km. The number of beams of the down-looking antenna drives the complexity of the Cookie. This conclusion holds regardless of the orbit inclination of the Cookie, its ascending node, and its other orbital parameters because they have little impact on the average number of reflection points and radio-occultation events.

The estimated numbers of up-looking beams (about 33) and down-looking beams (between 66 and 93) in the altitude range studied are average estimates obtained with the given assumptions and simple models, but, as it is shown in Table VII, they are within 4.3% from actual values.

B. On the Polarization of Signals and Antennas

The up-looking antenna of a Cookie receives only direct signals. As the transmitted polarization of GNSS satellites is right hand circular polarization (RHCP), this is the preferred polarization for the up-looking antenna. However, some applications, like biomass or ocean wind direction retrieval, do benefit from polarimetric observations for which it is necessary to know the amplitude of the component transmitted in left hand circular polarization (LHCP). For this reason, the polarization of the up-looking antenna of a Cookie will, in general, provide the two circular polarizations, i.e., RHCP and LHCP.

The down-looking antenna receives direct, reflected, and backscattered GNSS signals, and for the same reasons must also be capable of receiving both LHCP and RHCP polarizations.

In relation to Fig. 4, GNSS satellites in the upper hemisphere will provide reflected signals, mostly in LHCP, in the region of nadir angles within $0 < \beta < \beta_x$. The angle β_x can be found using the spherical mirror (5)

$$c_4 t^4 + c_3 t^3 + c_2 t^2 + c_1 t + c_0 = 0 \tag{11}$$

with the following coefficients:

$$\begin{aligned} c_0 &= (a - 2R_E)b \qquad c_1 = 2R_E a + 4b^2 \\ c_2 &= -6ab \qquad c_3 = 2R_E a - 4b^2 \\ c_4 &= (a + 2R_E)b \end{aligned} \tag{12}$$

where

$$a = \sqrt{(H-h)(H+h+2R_E)} \qquad b = R_E + h \tag{13}$$

TABLE II
MAXIMUM NADIR ANGLE β_x FOR REFLECTED SIGNALS ORIGINATED FROM A GNSS SATELLITE IN THE UPPER HEMISPHERE AND CORRESPONDING INCIDENCE ANGLE i_x AS A FUNCTION OF ORBITAL ALTITUDE (SEE FIG. 4)

h	β_x	i_x	β_y
400	66.9	77.9	70.2
800	58.1	72.9	62.7
1300	50.2	67.7	56.1

The nadir angle toward the Earth horizon β_y is given for reference. All angles are in degrees.

and

$$\tan\beta_x = \frac{1-t^2}{\left(1+\frac{h}{R_E}\right)(1+t^2) - 2t}. \tag{14}$$

The corresponding incidence angle is [5]

$$i_x = \beta_x + \tan^{-1}\left(\frac{1-t^2}{2t}\right). \tag{15}$$

Table II provides the values of β_x and i_x for the three different orbital heights of Table I, together with the Earth horizon nadir angle β_y (see Fig. 4). Table II shows that the reflected signals produced by the GNSS satellites in the upper hemisphere cover most of incidence angles (up to 68° or 78° incidence depending on orbital height).

The GNSS satellites located between points T_x and T_y in the lower hemisphere generate reflection points in the angular range $\beta_x < \beta < \beta_y$, producing reflected signals with a strong RHCP component because of the grazing geometry (large incidence angle). Even though the angular extent $\beta_y - \beta_x$ is relatively narrow, of just some degrees (see Table II), the number of reflection points M_y provided by the GNSS satellites in the lower hemisphere is rather high (see Table I), in particular for the higher orbit.

GNSS satellites within $\beta_y < \beta < \beta_z$ correspond to setting and rising GNSS satellites, and thus, used for radio-occultation. Their reflected signals come at a very grazing angle, within the same angular range, and mostly RHCP polarized.

C. Full-Pol Front-End Architecture

It follows from the previous section that to perform reflectometry and radio-occultation in parallel, it is necessary to receive the LHCP reflected and the RHCP rising/setting signals simultaneously through the down-looking antenna. Hence, the down-looking antenna not only has to have both polarizations, but it has to provide them in parallel. Otherwise, either the reflected or the radio-occultation signals would not be received with the correct polarization.

The up-looking antenna, instead, is not required to deliver both polarizations in parallel, as the residual LHCP component of the direct signals needs to be known only for some reflectometry applications but not for radio-occultation. For example, for wind direction and biomass determination, a sequential acquisition of both polarizations suffices, which is a good compromise between performance and complexity.

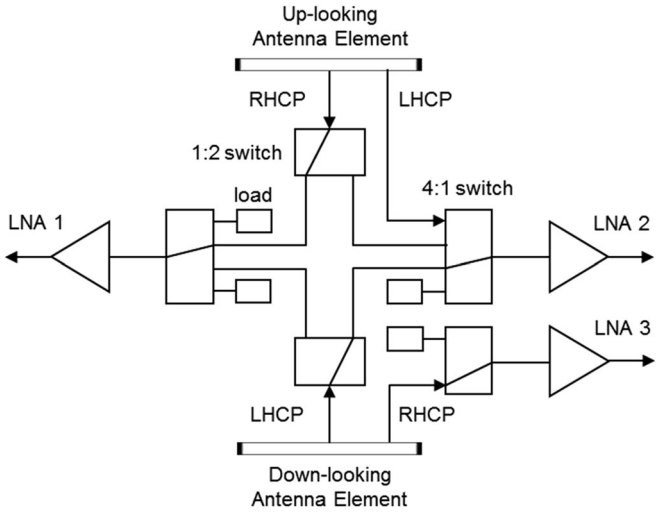

Fig. 5. Front-end for every antenna element pair of the Cookie.

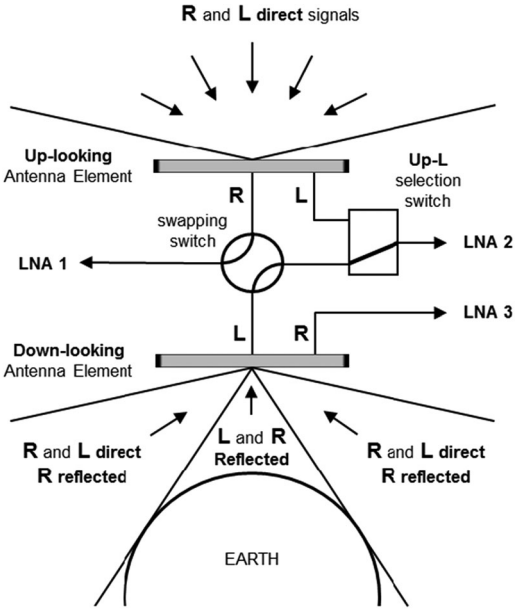

Fig. 6. Targeted polarization signals and its routing through the Cookie front-end enabling GNSS reflectometry and radio-occultation simultaneously.

This section presents a front-end architecture which can measure the two circular polarizations of the down-looking antenna elements in parallel, and the two polarizations of the up-looking antenna sequentially. The front-end also provides the means to remove instrumental delay errors and to carry out precise amplitude calibration, as explained later.

The proposed front-end architecture for the Cookie is shown in Fig. 5. Only the circuit for one frequency channel is shown. An identical one is used for a second channel, as dual-frequency observations are necessary to correct for the ionospheric delay (all GNSS systems transmit in at least two frequencies). The two front-ends are independent from each other as it is assumed that the antenna elements provide separate outputs for each of the two frequency channels.

Direct RHCP signals from GNSS satellites in the upper hemisphere are routed, by means of a 1:2 switch, toward low-noise amplifiers LNA1 and LNA2. Similarly is done with the forward- and backward-reflected LHCP signals captured by the down-looking antenna elements. In combined operation with the 1:2 switches, a second pair of 4:1 switches allows swapping the up- and down-looking antenna elements with the LNA1 and LNA2 amplifiers, to remove any instrument delay and perform accurate ranging. Matched loads at the inputs of the 4:1 switches, together with views of the cold sky, are used to calibrate the gain of each receiver chain accurately, end-to-end, except for the antenna directivity, which has to be characterized through ground tests.

Direct signals from rising and setting GNSS satellites are received through the RHCP radio-occultation port of the down-looking antenna elements. These RHCP direct signals are captured in parallel to the reflected ones in LHCP thanks to a third low noise amplifier LNA3. The LNA3 signal path, parallel to LNA1 and LNA2, enables simultaneous operation of reflectometry and radio-occultation. It also allows measuring the depolarization of direct signal traversing the atmosphere due to precipitation [33].

It is worth noticing that, because there is only one switch between the RHCP port of the down-looking antenna element and the LNA3 amplifier, radio-occultation signals are received with maximum sensitivity, and moreover, they do not undergo any antenna–amplifier swapping.

More generally, any direct RHCP signal from any GNSS satellite in the lower hemisphere, as well as its corresponding reflected signal (mostly RHCP polarized because of the grazing angle of the reflection), can be received through the RHCP port of the down-looking antenna elements. In turn, this saves the need for any calibration of the instrumental delay in reflectometry at grazing angle, as both direct and reflected signals go through the same electronics chain.

The RHCP port of the down-looking antenna elements is also used to capture the RHCP component of the forward- and backward-reflected signals corresponding to GNSS satellites in the upper hemisphere. This capability is important in some applications, as mentioned earlier. For the same reason, the up-looking antenna elements are provided with an LHCP output port to receive the cross-polar component of the direct GNSS signals in the upper hemisphere. The cross-polar signal is routed, through one of the 4:1 switches, toward LNA2. In normal operation, only from time to time, and just as much as needed to get the reference level of the cross-polar signal, the LHCP output of the up-looking elements is to be selected in place of its RHCP output.

Although the front-end circuit of Fig. 5 allows to receive, in parallel, the RHCP and LHCP components of the signals incident upon the up-looking antenna elements (at the expense of receiving only one polarization through the down-looking antenna), such configuration might seldom be used.

As a summary of this section, Fig. 6 shows a simplified diagram of Fig. 5 with the targeted polarization of the signals and its routing through the Cookie front-end.

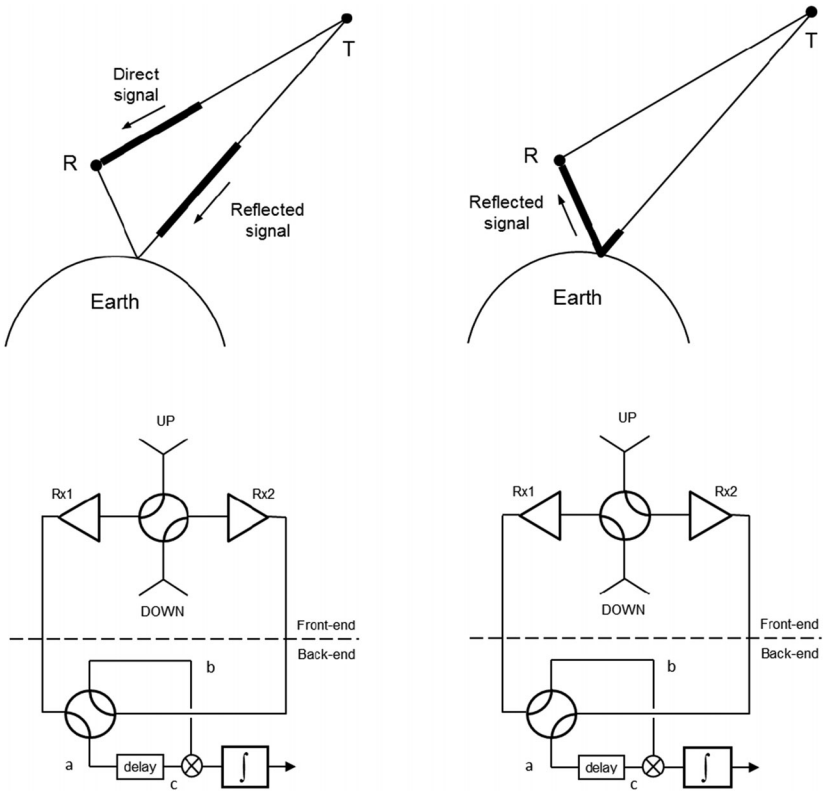

Fig. 7. Left panel: Direct signal is routed toward receiver branch Rx1. Right panel: Corresponding reflected signal is also routed to Rx1.

D. Delay Calibration

One of the design drivers of the Cookie front-end has been to enable the self-calibration of instrumental delays, in combined operation with a correlator circuit at the back-end, for the precise ranging of reflected signals. This is achieved by the *swapping* technique, first introduced in [24], successfully tested in the laboratory [37] and developed further here. The swapping technique is illustrated in Fig. 7, which includes a simplified diagram of the front-end of Fig. 5 and the back-end correlator. In the left panel of Fig. 7 the direct signal, entering through the up-looking antenna, is routed toward receiver branch Rx1 while the corresponding reflection is still traveling along its propagation path. In the right panel it is seen how as soon as the reflected signal arrives to the down-looking antenna, the receiver routing is swapped, so that it goes through the same receiver branch as the direct signal. In this way both signals, direct and reflected, undergo the same instrumental delay, and the relative timing between them is preserved, achieving effectively, a self-calibration of any instrumental delay errors.

The second receiving chain, Rx2, is there to perform continuous observations, that is, to capture the direct signal while Rx1 is being used for the reflected signal. The swapping technique is not required for the RHCP signals from GNSS satellites in the lower hemisphere as in this case, both the direct and reflected signals are measured through the same down-looking antenna and receiving chain, LNA3, in Fig. 5.

Fig. 8 illustrates the complete swapping technique with a time diagram. The back-end correlator unswaps the signals to separate the direct and the reflected portions, delays the direct signal to match the reflected one, and finally correlates portions of the signals which have gone through the same receiving branch.

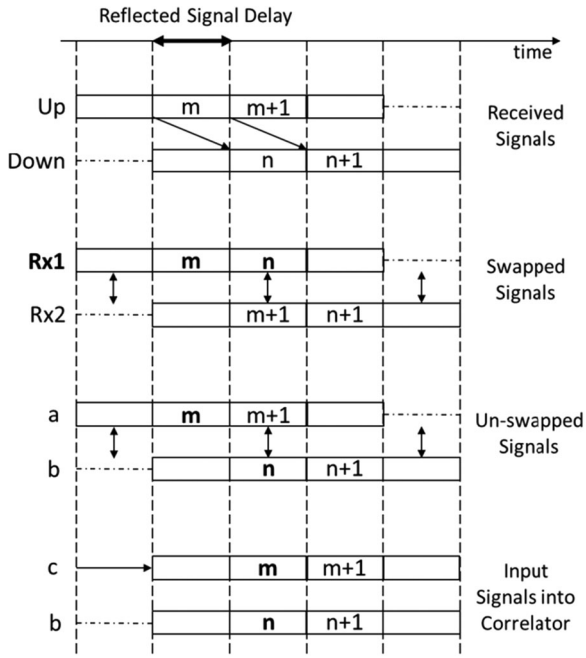

Fig. 8. Swapping technique: antennas and receivers are swapped with a period equal to the delay of the reflected signal. The correlator unswaps the signals to separate them prior to the correlation. The signal portions which are correlated went always through the same receiver branch (bolded segments through Rx1; unbolded ones through Rx2).

TABLE III
REFLECTED-TO-DIRECT SIGNAL DELAY (ALL DELAYS IN KM) AS A FUNCTION OF COOKIE ORBITAL HEIGHT, FOR THE FOLLOWING INCIDENCE ANGLES (FROM LEFT TO RIGHT): NADIR, 45°, INCIDENCE ANGLE i_h AT WHICH THE DELAY IS HALF ITS VALUE AT NADIR, i_m AT WHICH THE GNSS SATELLITE IS AT THE MASK ELEVATION ANGLE, AND i_x AT THE ANTENNA HORIZON

h	$i = 0°$	$i = 45°$	$i = i_h$	$i = i_m$	$i = i_x$
400	800	542–546	400	271–266	110–108
			$57° – i = 57.3°$	66.5°–67.1°	110–108
800	1600	1046–1059	800	618–604	311–302
			55°–55.5°	61.7°–62.7°	
1300	2600	1633–1665	1300	1116–1082	634–609
			53.1°–53.9°	57.3°–58.88°	634–609

The range of delays (and incidence angles in the third and fourth columns) indicates the extreme values across all GNSS constellations (left value is for GLONASS and right value is for overlay satellites at GEO orbit).

Ideally, the swapping period must equal the delay of the reflected signal. This delay is twice the orbital height of the Cookie, $2h$, when the GNSS satellite is at zenith, regardless of the GNSS system it belongs to, or whether it is an overlay satellite in the geostationary (GEO) orbit. However, for any other position of the GNSS transmitter away from zenith, in the upper hemisphere, the corresponding delay of the reflected signal is shorter than the zenithal delay, and does depend on the elevation angle and orbital height of the navigation satellite. In all cases, the delay of the reflected signals corresponding to GNSS satellites in the upper hemisphere is maximum at zenith and minimum at the antenna horizon.

Table III gives the values of the delay of the reflected signals (with respect to the direct signals) for the 3 orbital heights of the Cookie under consideration at several incidence angles: $i = 0°$ for a GNSS satellite at zenith, $i = 45°$ which defines the limit of the field of view around nadir in GEROS-ISS, $i = i_h$ which is the incidence angle at which the delay is half of its value at nadir, $i = i_m$ being the incidence angle for a GNSS satellite at the mask elevation angle, and finally, $i = i_x$ which is the incidence angle shown in Table II for a GNSS satellite at the antenna horizon. The delay of the reflected signals is given for two extreme cases: GLONASS, the GNSS constellation with lowest orbital height, and GEO overlay satellites, which are the GNSS transmitters with maximum orbital height. Table III also provides the incidence angles i_h and i_m for the same extreme cases.

Table III shows that the variation of the delay of the reflected signal with the elevation of the GNSS satellite is important, of the order of 32% ($h = 400$ km) or 37% ($h = 1300$ km) between nadir and 45° incidence, and the dispersion of such variation across GNSS constellations is negligible, of about 1% or less. Therefore a different swapping period should be used depending on the elevation angle of the GNSS satellites. This is not possible, though, for the swapping is performed on the outputs of the up- and down-looking antenna elements, which contain the composite signal from all GNSS satellites in their field of view. Consequently, it has to be accepted that a single swapping period be used. Such value $T_{\rm swap}$ may be found after some

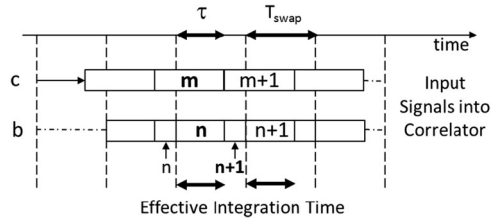

Fig. 9. Input signals into the correlator for a GNSS satellite at an elevation such that the delay of its reflected signal relative to the direct one is smaller than the swapping time, i.e., $t < T_{\rm swap}$: the effective integration time becomes smaller than the swapping period as only signal parts which went through the same receiver chain provide a valid cross correlation (bolded segments went through Rx1; unbolded ones through Rx2).

TABLE IV
COLUMNS 1 AND 2: SWAPPING TIME $T_{\rm swap}$ (IN KM) AS A FUNCTION OF THE ORBITAL HEIGHT; COLUMN 3: DEVIATION FROM THE SWAPPING PERIOD OF THE DELAY OF THE REFLECTED SIGNAL RELATIVE TO THE DIRECT ONE AT FOUR INCIDENCE ANGLES (IN KM); COLUMN 4: CORRESPONDING RANGE PRECISION DEGRADATION FACTOR

		Delay Deviation From $T_{\rm swap}$				Range Precision Degradation			
h	$T_{\rm swap}$	$i = 0°$	$i \sim 38°$	$i \sim 45°$	$i = i_h$ ($\sim 55°$)	$i = 0°$	$i \sim 38°$	$i \sim 45°$	$i = i_h$ ($\sim 55°$)
400	600	+200	0	−56	−200	11.8%	0.0%	5.0%	22.5%
800	1200	+400	0	−148	−400	11.8%	0.0%	6.8%	22.5%
1300	1950	+650	0	−301	−650	11.8%	0.0%	8.7%	22.5%

optimization process (such as, for example, to get the best overall ocean altimetry) but for the purpose of showing the impact of having a single value, $T_{\rm swap}$ will be chosen equal to the average value of the reflected-to-direct signal delays at incidence angles $i = 0°$ and $i = i_h$. The incidence angle at which such delay equals $T_{\rm swap}$ depends on the particular GNSS constellation, but it is about $i_{\rm swap} \sim 38°$.

With this assumption, the timing diagram of Fig. 8 holds true only for a GNSS satellite at an elevation angle corresponding to an incidence angle at the specular point of $i_{\rm swap} \sim 38°$. For GNSS satellites at any other elevation, the relative delay of the reflected signals is shorter or longer than $T_{\rm swap}$, and only the fraction of the swapping period for which the inputs to the correlator have gone through the same receiver chain, as depicted in Fig. 9, can effectively be used to cancel instrumental delays out in the correlation.

The first two columns in Table IV show the chosen swapping period $T_{\rm swap}$ for the three different orbital heights. The baseline operation of the Cookie would consist in having such swapping time applied automatically and continuously. This can be done through the instrument control unit actuating on the switches of the front-end. The correlator in the back end would have to select the effective integration interval, within each swapping period, for each particular GNSS satellite as a function of its elevation angle. As mentioned earlier, the value of $T_{\rm swap}$ should be the result of an optimization process to obtain the best ranging overall, given the probability density function of the average number of GNSS satellites at a given elevation angle. The selected swapping period adopted in Table IV is only for

the purpose to show the order of magnitude of the impact in the range precision.

The degradation in range precision comes from the shorter effective integration time available for GNSS satellites whose relative delay (reflected to direct signal) is shorter or longer than the swapping period T_{swap}. The third column of Table IV shows such relative delay deviations from T_{swap} for different incidence angles. Assuming that the coherence time is significantly shorter than the swapping period and that the SNR is high enough so that the range precision is dominated by the number of incoherent samples, then, the degradation factor in range precision is proportional to the square root of the ratio between the effective integration time and the swapping period. As shown in the last column of Table IV, the range precision degradation factor is of about 12% at nadir, goes through a minimum of 0% around 38% incidence angle and increases up to 22.5% at an incidence of about 55°.

It is therefore concluded, that the degradation of the ranging precision with the incidence angle induced by the use of a single swapping period is a graceful one, reaching no more than 22.5% over a wide field of view of about 55° incidence angle. For the highest orbit ($h = 1300\,\mathrm{km}$) such field of view comprises specular points as far as 1276 km from the subsatellite point, equivalent to an access swath of about 2552 km.

A couple of remarks are presented before concluding this section. As happens to the delay, the estimation of other parameter of the correlation waveform, such as the amplitude, important in scatterometry applications, will suffer from the reduction in effective integration time due to the swapping. It is here assumed, without further analysis, that the relative order of magnitude of such degradation is similar to that of the delay, and hence, acceptable. This is an implicit assumption that the Cookie can be used for scatterometry observations while in swapping mode.

The final remark is about the fact that due to the oblateness of the Earth, the height of the Cookie over the Earth surface h will vary by some 43 km (the effect on h of the eccentricity e of the Cookie orbit is negligible, for typical values below $e < 0.002$). This represents an appreciable change in the delay of the reflected signals along the orbit (about 11% for the lowest orbit of 400 km). However, being common to all GNSS satellites, this variation can be easily compensated for by dynamically adjusting the swapping period along the flight. This imposes a noncritical requirement on the instrument aboard the Cookie, that of continuously adjusting the swapping period as a function of the orbital height, which shall be assumed fulfilled, removing any degradation factor in addition to the one just discussed.

E. Amplitude Calibration

Amplitude calibration is particularly important for scatterometry applications, but it may also have an impact in the accuracy of altimetry and radio-occultation observations. Generally speaking, the problem to solve is that of measuring the embedded complex voltage antenna pattern of every element of the up- and down-looking arrays of the Cookie, and the voltage gain of every receiving branch attached to them. The former can be done on ground by careful characterization of every embedded element antenna pattern, using standard procedures, and will not be discussed further here. The latter needs to be implemented in flight to remove orbital and seasonal physical temperature effects, and for this purpose, the payload aboard a Cookie includes the following three key features: first, matched loads in the front-end of Fig. 5 whose physical temperature is monitored; second, the capability to control the switches of every single front-end individually; and third, a power detector circuit in the back-end with a variable attenuator which allows to measure received power for two different values of attenuation. These features implement in practice the four-point calibration method described in [36].

An alternative way to accomplish amplitude calibration by the Cookie is using the *peak ratio*. The peak ratio is a self-calibration technique consisting of forming the ratio of the peak of the cross correlation between the direct signal and an on-board generated clean code replica to the peak of the cross correlation between the reflected signal and the same clean code replica. This method assumes that both the direct and the reflected signals have been received through the same electronics, and the relative delay between the reflected signal and the direct signal is longer than the width of the autocorrelation function of the direct signal (typically about 1 C/A code, i.e., 300 m), so that the two peaks of the two mentioned cross correlations (direct-replica and reflected-replica) are well separated. The first assumption is fulfilled for GNSS transmitters in the upper hemisphere through the swapping technique, and for those in the lower hemisphere thanks to the fact that both the direct and the reflected signals are captured by the same receiver. The second assumption is satisfied for all reflection points except for those whose direct signal passes very close to the Earth surface, for which the relative delay between the reflected signal and the direct one is less than 300 m. The peak ratio technique still requires to be completed with the ground characterization data of the antenna patterns and also, the amplitude behavior of the phase shifters of the beamformers, as their setting is different when receiving the direct signal or the reflected signal. Because the peak ratio can be rather small, of the order of -30 dB or even lower, it is required to perform the ratio after having removed thermal noise and speckle effects, which in practice means an integration time of the order of 1 s.

F. Nominal Measurement Mode of the Cookie

Besides the necessary calibration modes, the Cookie is designed to work in a single nominal measurement mode, which is to provide, in parallel, all the measurements listed in Table V, including both GNSS-R and GNSS-RO observations.

The nominal measurement mode of the Cookie, which does not exclude other alternative modes, is explained further. In doing so, it is practical to distinguish between observations obtained using transmitters in the upper hemisphere, and those from transmitters in the lower hemisphere.

1) Observations Using Upper Hemisphere GNSS Transmitters: These comprise forward and backward reflectometry in all possible polarization combinations.

a) Direct RHCP Against Reflected LHCP: For ranging applications, the RHCP direct signals of the B_{x} up-looking

TABLE V
OBSERVATIONS PROVIDED BY THE COOKIE IN ITS MEASUREMENT MODE (UP = RECEIVED THROUGH THE UP-LOOKING ANTENNA; DOWN = RECEIVED THROUGH THE DOWN-LOOKING ANTENNA—SEE FIG. 2)

	Up		Down					
			Reflected					
	Direct		Forward		Backward		Direct	
Application	R	L	R	L	R	L	R	L
1) Around-nadir Altimetry	X			X				
2) Grazing Altimetry			X				X	
3) Forward Scatterometry RL	X			X				
4) Forward Scatterometry RR	X		X					
5) Forward Scatterometry LL		X		X				
6) Forward Scatterometry LR		X	X					
7) Backward Scatterometry RL	X					X		
8) Backward Scatterometry RR	X				X			
9) Backward Scatterometry LL		X				X		
10) Backward Scatterometry LR		X			X			
11) Radio-occultation (interference)	X						X	
12) Precipitation							X	X

TABLE VI
PARAMETERS USED IN THE SIMULATION OF THE THREE COOKIE CONSTELLATION

Parameters		Value
GNSS Constellation	GPS	31
	GLONASS	28
	GALILEO	27
	BeiDou	35
	SBAS	11
	Total GNSS Transmitters	132
Cookie Constellation	Number of Cookies	3
	Architecture	Walker 3/3
	Orbit Altitude	1300 km
	Orbit Inclination	55°
Reflection Points	Near Nadir Reflection	0° to 45°
Incidence Angle	Grazing Reflection	60° to 85°
Radio-occultation	Rising	−45° to +45°
Azimuth Angle	Setting	−135° to +135°
(0° = velocity vector; ±180° = antivelocity)	Side-looking	−45° to −135° +45° to +135°

beams and the LHCP forward reflected signals of their associated down-looking beams have to be swapped across LNA1 and LNA2, to then being unswapped prior to getting cross correlated with each other, so that any instrumental delay is automatically removed.

Because the delay calibration is critical for ranging observations, it is proposed that, in nominal operation, the Cookie performs antenna–receiver swapping continuously in an automatic way. This is compatible with doing, in parallel, reflectometry at grazing angles and radio-occultation, for the latter measurements are carried out through the dedicated branch LNA3 decoupled from the swapping switch (see Figs. 5 and 6).

This combination of signals, direct RHCP against reflected LHCP, is also required for scatterometry observations in all B_x beams.

b) Direct LHCP Against Reflected LHCP: For the benefit of scatterometric applications it is proposed that periodically, perhaps for 10% of the time and for a duration of one half-swapping cycle, for example, the LHCP polarization component of the direct signal (B_x beams) is selected as output of LNA2, and then correlated against the corresponding LHCP forward reflected signal, available at the output of LNA1. Alternatively a scatterometric mode could be devised with increased time spent in measuring the LHCP direct component.

c) Direct RHCP Against Reflected RHCP: For scatterometric applications, the direct RHCP signal, which is available at the output of either LNA1 or LNA2, is unswapped and correlated with the RHCP forward ($B_{\rm x}$ beams) or backward ($M_{\rm x1}$ beams) reflected signal provided by LNA3.

d) Direct LHCP Against Reflected RHCP: For scatterometry, when the direct LHCP signal is selected at the output of LNA2, it is correlated with the RHCP forward ($B_{\rm x}$ beams) or backward (M_{x1} beams) reflected signal provided by LNA3.

2) Observations Using Lower Hemisphere GNSS Transmitters: These comprise forward reflectometry at grazing angle and radio-occultation, in specific polarization combinations of scientific interest.

a) Direct RHCP Against Reflected RHCP: For grazing angle ranging, the RHCP component of the forward reflected signals ($M_y - M_{\rm ym} - M_{y1}$ beams), captured through the down-looking beams of the same polarization, and available at LNA3 output, is cross correlated with the corresponding RHCP direct signal ($M_y - M_{\rm ym} - M_{y1}$ beams).

b) Direct RHCP: The direct RHCP signals of rising or setting GNSS satellites ($M_{\rm y1}$ beams) are cross correlated with stored reference signals using interferometric radio-occultation [32] or with clean replicas for conventional radio-occultation. Zenithal reference signal acquisitions are preferred over top of the atmosphere acquisitions in interferometric radio-occultation, in particular for orbital heights below $h = 800$ km.

c) Direct RHCP Against Direct LHCP: For atmospheric precipitation observations, the LHCP component of the direct signal of a rising or setting GNSS satellite ($M_{\rm y1}$ beams) is captured through the down-looking beams of the same polarization, whose signal is swapped between LNA1 and LNA2 outputs. Unswapping these two signals allows to reconstruct the original LHCP signal which is then cross correlated against the RHCP direct signal, available at LNA3 (M_{y1} beams).

G. Timing, Positioning, and Precise Orbit Determination

For several of the applications the Cookie is intended for, as altimetry and radio-occultation, it is important to provide accurate timing, positioning, and the means to recover in post-processing, at centimeter level, the position of the antenna phase center. For this purpose, the signal of the center element of up-looking antenna array of the Cookie is used to feed the input of a dual frequency GNSS navigation receiver. In addition, the center element of the down-looking antenna is replaced by a laser retro-reflector for laser ranging from ground, used for accurate positioning verification and orbit determination. This is the approach adopted for the GEROS-ISS mission concept.

H. Block Diagram of the GNSS Remote Sensing Payload

The high level block diagram of the instrument on board the Cookie is presented in Fig. 10. It produces all measurements indicated in Table V, effectively in parallel. The RHCP and

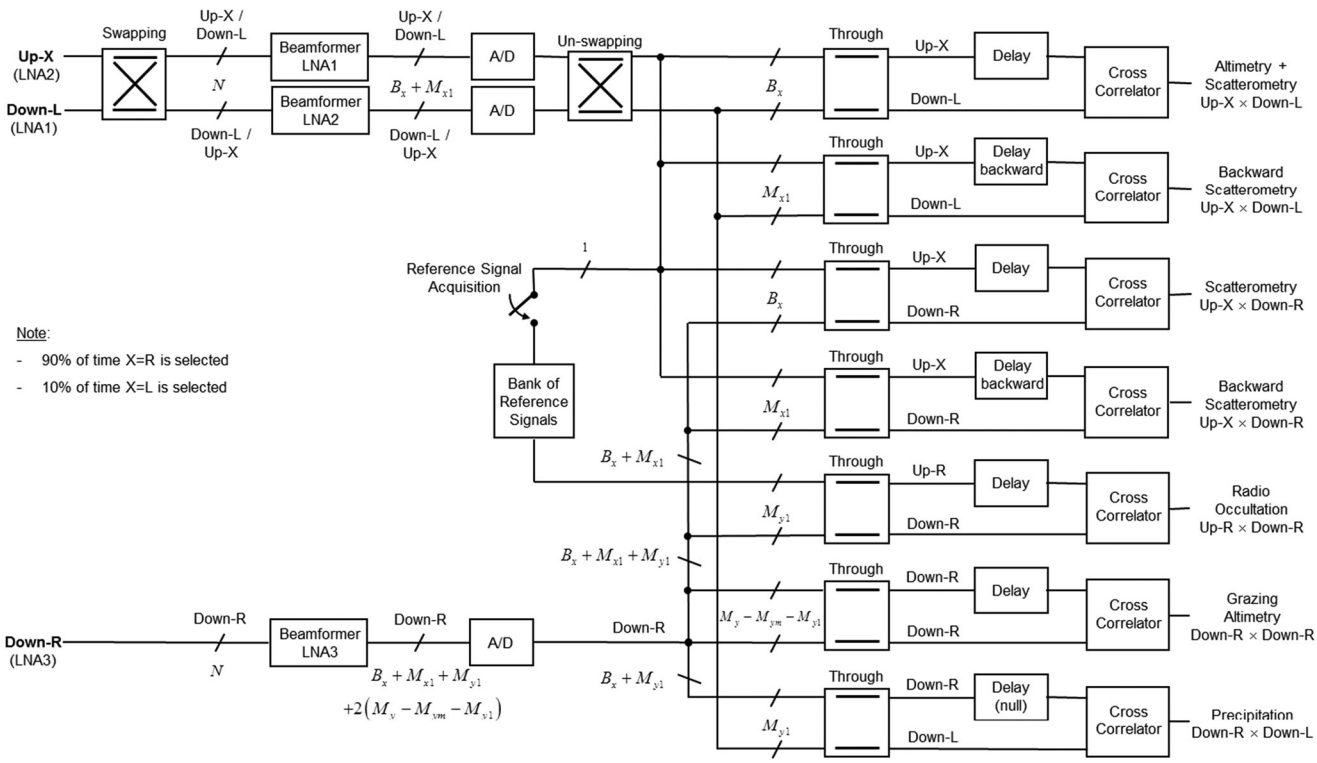

Fig. 10. Conceptual block diagram of the Cookie GNSS remote sensing payload.

the LHCP polarizations of the up-looking antenna are selected sequentially, in typical 90% and 10% time shares, respectively, at a rate fast by comparison with the dwell time corresponding to the spatial resolution.

I. Data Rate

A rough estimation of the output data rate of the Cookie is given here based on the GEROS-ISS mission concept, described in [31]. GEROS-ISS payload is required to have an average output data rate of no more than 1 Mb/s to provide observations of four events in parallel and continuously, be them reflection points, radio-occultations or a combination of both. This leads to 250 kb/s per event. Assuming the same data rate per event for the Cookie as for GEROS-ISS, and taking into account that the Cookie has to handle an average number of simultaneous observations of $M_{\rm obs} = 73$ (refer to (16) and Table VII), then its average output data rate must be 18.25 Mb/s. For an average contact time to ground stations of 5% of the flight time, a downlink data rate of 365 Mb/s is adequate. Adding a margin of 20% yields 450 Mb/s, which is in the limit of an X-band downlink, but certainly well within the capability of a Ka-band downlink.

TABLE VII
COMPARISON BETWEEN MODELED [SEE (5)–(10)] AND SIMULATED GNSS TRANSMITTERS SKY DISTRIBUTION, NUMBER OF BEAMS [SEE (1) AND (2)] AND NUMBER OF OUTPUT OBSERVATIONS

Modeled	M_x	M_{x1}	$M_{\rm xm}$	M_y	M_{y1}	$M_{\rm ym}$	B_x	B_y	Number of Output Observations
Simulated Deviation									
400 km	49.6	29.8	15.5	23.6	9.5	17.7	34	66	70
	51.2	*31.0*	*15.6*	*21.9*	*8.7*	*16.3*	*36*	*69*	*72*
	−3.1%	**−3.9%**	**−0.7%**	**7.9%**	**8.5%**	**8.5%**	**−4.2%**	**−4.0%**	**−3.3%**
800 km	48.7	22.9	15.4	33.1	6.0	17.7	33	81	72
	50.3	*23.4*	*15.5*	*30.8*	*5.8*	*16.4*	*35*	*81*	*73*
	−3.2%	**−2.4%**	**−0.9%**	**7.5%**	**2.7%**	**7.9%**	**−4.2%**	**−0.2%**	**−1.4%**
1300 km	47.5	17.5	15.2	41.5	4.4	17.7	32	93	74
	49.1	*17.4*	*15.4*	*39.3*	*4.6*	*16.5*	*34*	*92*	*74*
	−3.4%	**0.4%**	**−1.4%**	**5.7%**	**−3.8%**	**7.0%**	**−4.3%**	**1.1%**	**−0.4%**

IV. SPACECRAFT FEATURES OF THE COOKIE

The Cookie is arbitrarily defined as a spacecraft which can be enclosed within a right circular prism section of minimum volume with a height no longer than one-fourth of its diameter (see Fig. 11, top). The Cookie is divided in two parts, for the platform and the payload. This split is important as the manufacturing, assembly and testing of the two parts, typically done by different industries, can be carried out in parallel, until final integration at satellite level.

The primary structure of the Cookie is formed by a central cylindrical section, divided in two halves, for the platform and payload assemblies (see Fig. 11, top). When assembled together, both ends of the main structure serve as mechanical interface rings, allowing Cookies to be piled up vertically inside a rocket. The one-fourth height-to-diameter ratio of the Cookie ensures that at least eight Cookies can be packed in most launcher fairings (see Fig. 11, middle). During launch, the loads are transferred through the primary structure of the stacked Cookies into the launcher interface. The ring ends are provided with proper

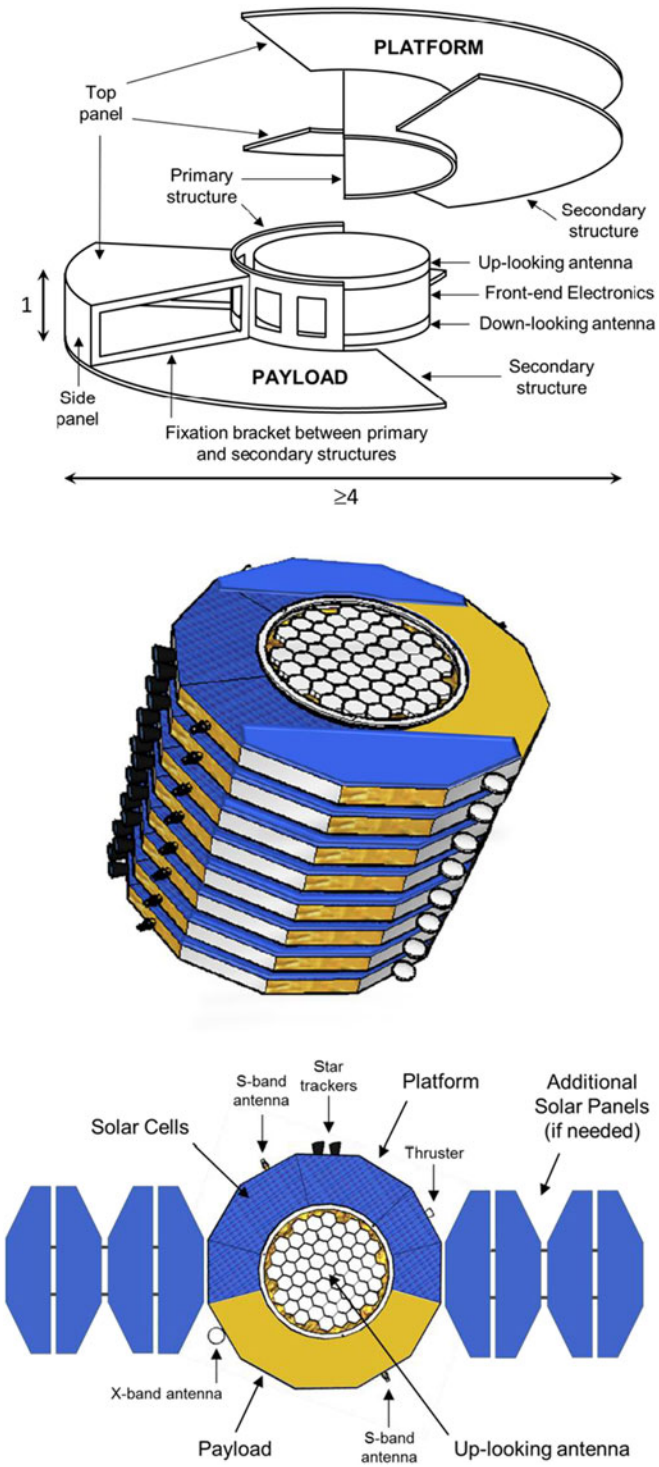

Fig. 11. Top: Structure of Cookie with platform-payload split-assembly concept. Middle: Eight Cookies piled in launch configuration. Bottom: Solar cells disposition, including additional solar wings.

hold down and release mechanisms, preferably of the nonexplosive type, to avoid any mechanical shock onto the nearby antenna front-end electronics.

The payload primary structure half-hosts the up- and down-looking antennas together with their front-end electronics (see Fig. 11, top). All this electronic equipment is held onto a secondary structure tray, attached to the primary one. The corresponding harness is routed through openings properly located in the cylindrical wall.

The secondary structure of both the platform and instrument assemblies is formed by one planar sheet extending orthogonally around the outer side of the cylindrical wall, and fixed rigidly to it with brackets or other suitable structural elements in the radial direction. The remaining payload electronics as well as the avionics and the propulsion system (if applicable) sit on this secondary structure.

The lateral and top sides of the Cookie assemblies are covered with light weight panels. The solar cells are body-mounted on the top panel of the platform. Alternatively, or if necessary, solar arrays can be arranged on deployable wings around the Cookie (see Fig. 11, bottom). The angle at which these wings open can be readily optimized for each particular orbit by adjusting the latching angle of their root hinge. Radiators are conveniently distributed in the lateral panels that face toward the cold sky.

Following the jettison of the shroud, the packet of Cookies remains attached to the last stage of the launcher until reaching the target orbit. Using power from its own battery, the Cookie at the top releases itself from the packet by activating its release mechanism. If needed, the last stage is made to point toward the Sun to have the solar cells of the Cookie at the top illuminated. The remaining Cookies are released one after the other at appropriate intervals in the same way the first one detached itself. The Cookies make their way to their final orbital position either by changing their cross section to the atmospheric drag with attitude maneuvers, or by using their own propulsion system, or carried by the last launcher stage.

The Cookie is flown nadir pointed using an active attitude control system. The geometry of the Cookie allows both the up- and the down-looking antennas to have virtually full 2π sr visibility without obstructions or multipath, except, perhaps, for a small intrusion of the solar wings. Cookies could be furnished with intersatellite link capability to cover disaster prevention and disaster early warning system applications.

The minimum diameter of the beamformer antenna for a Cookie flying in a low orbit (400 km) is of about 0.9 m, to guarantee a minimum SNR in the interferometric processor. For a high altitude (1300 km) the antenna size must be increased to about 1.4 m. The diameter envelope of the whole Cookie can be as big as that of the launcher fairing, which, as an example, for VEGA is near 2.3 m.

V. Simulation of a Three Cookie Constellation

To analyze the performances of the proposed concept, a constellation with three Cookies in LEO has been simulated. The main parameters of the simulation are summarized in Table VI. The simulation contemplates all GNSS satellites that should be available in the timeframe 2020: a total of 132 GNSS transmitters are expected. An implicit assumption is made here that the receiver on board the Cookie can track all available GNSS signals in the near future, which requires an access bandwidth of about 60 MHz in the lower navigation band (comprising GPS

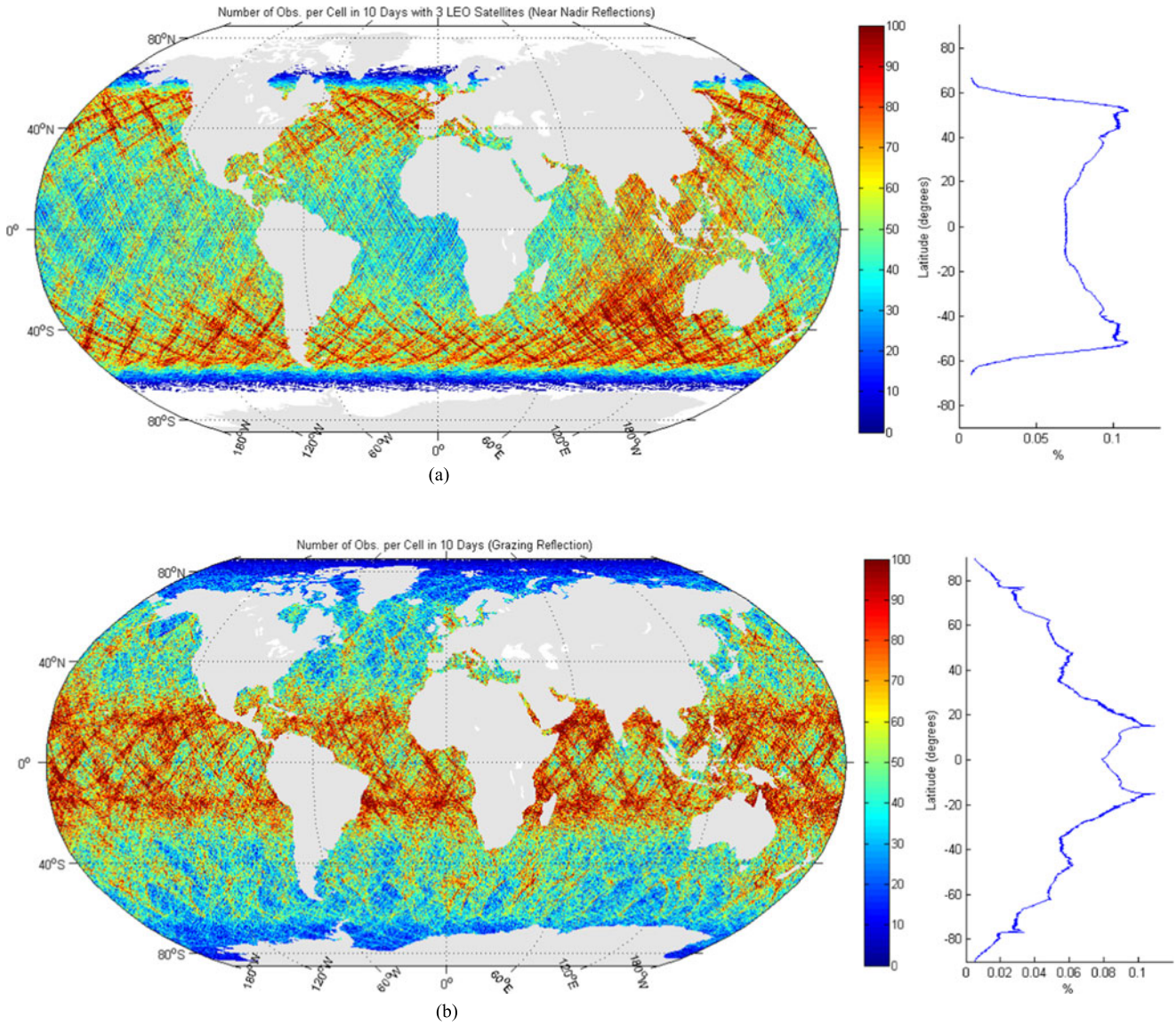

Fig. 12. Left plots: Global distribution of the number of 1-s GNSS-R observations per cell of $0.2^\circ \times 0.2^\circ$ (about $20\,\mathrm{km} \times 20\,\mathrm{km}$) provided by a three Cookie satellite constellation, accumulated over a period of 10 days. Right plots: longitudinal average as a function of latitude for (a) near nadir reflections and (b) grazing reflections. Color scale is in millions/day.

L5, Galileo E5, etc.) and 40 MHz in the upper band (GPS L1, Galileo E1, etc. assuming only CDMA signals are targeted. An interferometric receiver can intrinsically cope with all those signals while a clean replica based receiver requires a consolidated signal definition.

A. Number of Specular Points and Altimetric Precision

Specular reflection points are computed using the Cookie receiver and the GNSS transmitters positions derived from Two Line Element sets. The reflection opportunities that happen over a duration of 10 days have been analyzed in this study. As shown in Table VI, they have been classified in two groups: "near nadir" reflections, for which the incidence angle at the specular point is lower than 45° and "grazing" reflections, for which the incidence angle is between 60° and 85°. The reflected to direct path relative delay of nadir reflections is obtained from the position of the leading edge of the corresponding cross correlation power waveforms. For every near nadir reflection, one delay measurement is provided every 1 s, typically as a result of accumulating incoherently 1000 cross correlations of 1 ms each. For grazing reflections, the relative delay is derived from the phase at the peak of the 1-s cross correlation complex waveforms, as in grazing geometry the reflected signal has a strong coherent component. The upper limit of the incidence angle range for grazing altimetry, 85°, is chosen to remove the extreme grazing geometries (from 85° up to 90°) for which the atmospheric ray tracing models have too large errors.

By gridding the global ocean surface into small cells of $0.2^\circ \times 0.2^\circ$ in size (about 20 km × 20 km), the number of observations made over a simulation period of 10 days in each individual cell has been obtained. The count of 1 s near nadir and grazing altimetry observations per cell over the 10 day

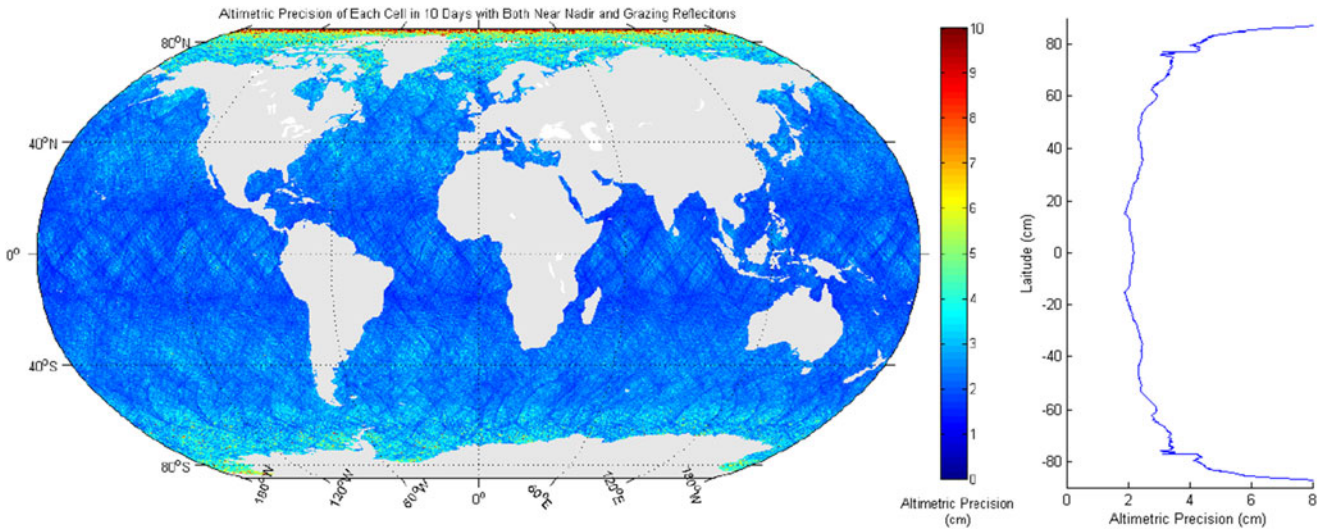

Fig. 13. Left: Global distribution of the precision in SSH measurements attained by the three Cookie satellite constellation after accumulating near nadir and grazing GNSS reflection observations over a 10 day period, and a spatial resolution of 20 km × 20 km. Right: Longitudinal average SSH precision as a function of latitude.

period is presented in the maps of Fig. 12(a) and (b), respectively. The latitudinal distribution of the observations is also presented. The number of grazing reflections (∼50 million/day), which has been computed considering a mask angle of 15° for both the up- and the down-looking antennas, is about two-fold that of near nadir reflections (∼25 million/day). It is also important to note the complete coverage of the poles by grazing altimetry observations.

For a first order sensitivity analysis, it has been simply assumed, based on the GEROS-ISS Phase A study, that an instrumental precision of 25 and 10 cm could be achievable by the 1-s observations of the near nadir and grazing reflections respectively. Adding 5 cm to accommodate some ionospheric residual error to the instrumental noise, 30 and 15 cm are assumed for the global precision of near nadir and grazing measurements, respectively. All these numbers come from analyses, simulations and experiments performed for GEROS-ISS or in relation to it, but can only be confirmed by the realization of such spaceborne mission itself. After 10 days, the precision of the sea surface height in each $0.2^\circ \times 0.2^\circ$ cell can be improved by averaging all the measurements taken in that cell (the number of which is found in Fig. 12). If it is assumed that the improvement is proportional to the square root of the number of observations then the resulting 10 day SSH precision is shown in Fig. 13. A value better than 4 cm is reached in each cell within a latitude range of ±80°, considering the contribution of both near nadir and grazing reflections. Certainly there are errors (orbital, instrumental, and propagation errors) which are partially correlated and do not reduce with the square root of the number of measurements. On the other hand, Optimal Interpolation or two-dimensional (2-D) Var Filters of current oceanography assimilation models have the ability to bit the square root of the number of measurements law. Therefore, the results shown in Fig. 13 intend to be more an indication of the sampling capability provided by the Cookie satellite concept than a real estimation of its SSH precision performance.

B. Number of Radio-Occultation Events

Regarding the radio-occultation observations, the simulator has provided the number of occultation events per day which the three Cookie satellite constellation is capable of. A map with the global repartition of these events as well as their latitudinal distribution is presented in Fig. 14. Rising (±45° around the velocity direction) and setting (±45° around the antivelocity direction) events are shown together, whereas side-looking (in any other azimuth angle) radio-occultations are given separately. The side-looking events can be captured by the Cookie thanks to its full azimuth coverage provided by the combination of its beamformer antenna and the spacecraft geometry (free of obstacles). Although till now there is little experience in exploiting side-looking radio-occultations, it is believed that in the future they can indeed be used for atmospheric sounding.

An average of 5530 GNSS-RO rising and setting events per day, together with 3420 side-looking radio-occultations, is obtained by the three Cookie constellation, which could supplement the RO data acquired with the existing and planned missions, such as COSMIC (∼1500 RO events per day) and COSMIC-2 (12 000 RO events per day).

C. Number of Observations and Comparison to Modeled Values

Using the simulator, the exact number of GNSS transmitters in the different sky regions (M_x, M_{x1}, M_{xm}, M_y, M_{y1}, and M_{ym}) has been computed and compared to their corresponding modeled values by (5)–(10), for the three orbit altitudes of interest. The result is shown in Table VII, which also provides the deviation in percent. The largest difference is of 8.5% and happens for the number of GNSS transmitters in the lower hemisphere at the lowest orbital height. For the highest orbit the biggest deviation is of 7%. Similarly the number of beams (B_x and B_y) necessary to track all reflection and radio-occultation opportunities has also been compared resulting in errors not greater than 4.3%.

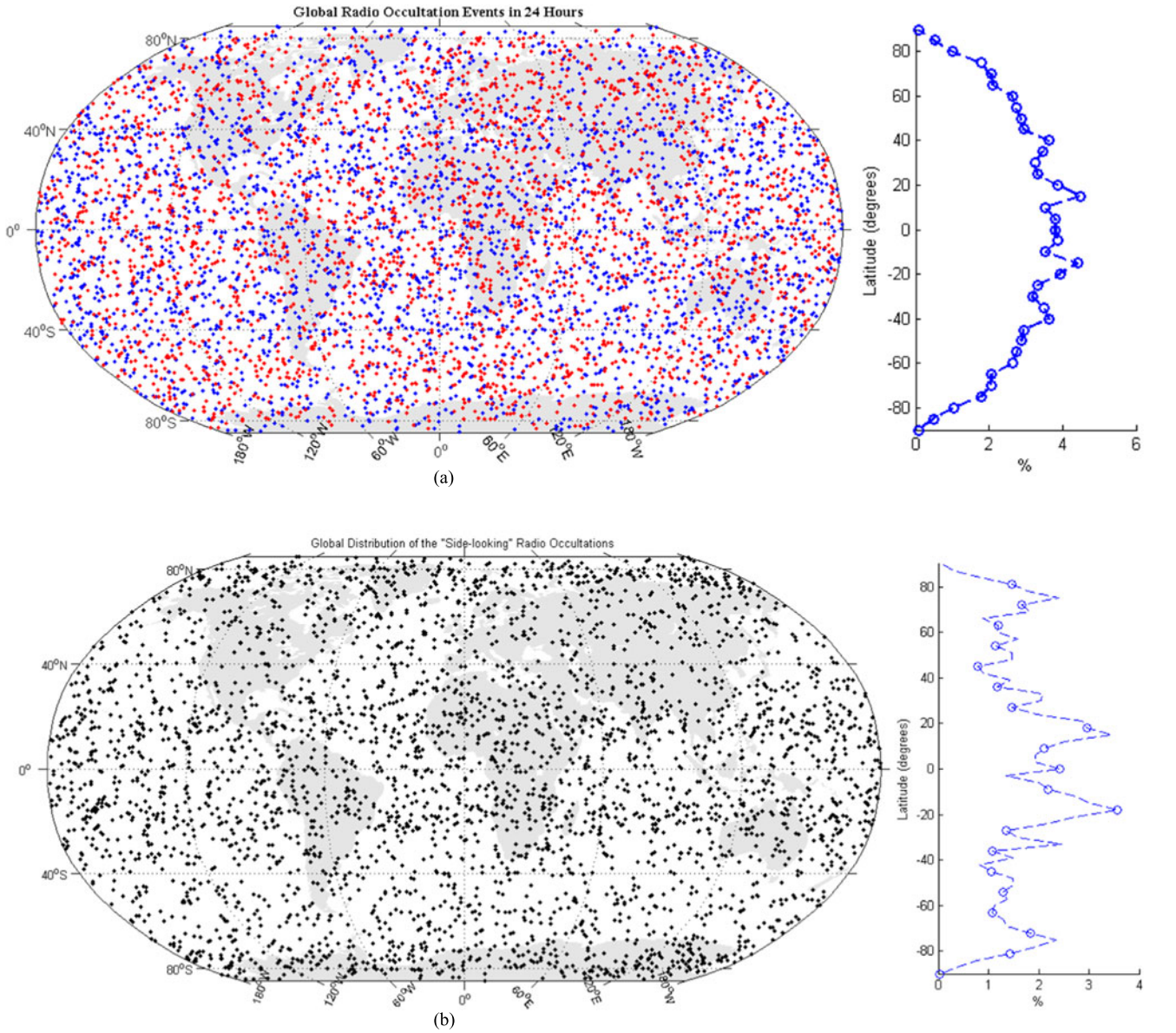

Fig. 14. Left: Global distribution of the radio-occultation events provided by a three Cookie satellite constellation over a period of one day (setting occultations in red, rising occultations in blue, in the top panel; side-looking radio-occultations in the bottom panel). Right: longitudinal average distribution as a function of latitude of rising and setting (top), and side-looking (bottom) radio-occultations.

The average number of simultaneous observations, $M_{\rm obs}$, including forward and backward near nadir reflections, grazing reflections, and rising, setting, and side-looking radio-occultations is given as follows:

$$M_{\rm obs} = (M_x + M_{x1} - M_{\rm xm}) + (M_y - M_{\rm ym}). \qquad (16)$$

This number sets the output number of measurements a Cookie can provide at any one time, on average. Modeled and simulated values of $M_{\rm obs}$ have been compared and provided in the last column of Table VII. The agreement is quite good, with deviations contained within 3.3% for all three orbital heights.

D. Cookie Performance Against Conventional Approaches

The altimetric performance of the Cookie can be compared against a conventional altimeter mission by assessing the 1-s altimetric precision $\sigma_{\rm h}$. Since the Cookie provides two types of observations (near nadir and grazing) with different precision, an overall altimetric precision shall be defined through the root mean squared combination of the individual values. Let σ_a and σ_b be the 1-s instrument precision for the near nadir and grazing altimetric measurements, respectively, and M_a and M_b the corresponding average number of simultaneous observations. Then, the global altimetric precision of the Cookie can be expressed by (Annex I)

$$\sigma_h = \sqrt{M_a + M_b}\left(\frac{M_a}{\sigma_a} + \frac{M_b}{\sigma_b}\right)^{-1}. \qquad (17)$$

A reasonable assumption for a first order assessment is to consider that all forward reflected signals originated from GNSS transmitters in the upper hemisphere generate near nadir type

TABLE VIII
1-S ALTIMETRIC PRECISION OF THE COOKIE COMPARED TO THAT OF A CONVENTIONAL ALTIMETER

	Cookie					Conventional	Ratio
Mask angle	σ_a	M_a	σ_b	M_b	σ_h	σ_{ho}	$(\sigma_{\mathrm{ho}}/\sigma_h)^2$
15°	25 cm	33	10 cm	18	2.3 cm	3 cm	1.7
5°	25 cm	33	10 cm	40	1.6 cm	3 cm	3.5

of observations, while all those linked to GNSS satellites in the lower hemisphere, except for the radio-occultation events, produce grazing type reflections. Under this assumption

$$\begin{aligned} M_a &= M_x - M_{\mathrm{xm}} \\ M_b &= M_y - M_{\mathrm{ym}} - M_{y1}. \end{aligned} \tag{18}$$

Table VIII provides the number of near nadir and grazing reflections, M_a and M_b, for two mask angles E_m of 15° and 5°, making use of (18) and Table VII, as well as the altimetric precision given by (17) for the instrumental noise assumed earlier, i.e., $\sigma_a = 25\,\mathrm{cm}$ and $\sigma_b = 10\,\mathrm{cm}$, respectively. Table VIII also gives the equivalent number of conventional altimeters, each one having 3 cm 1-s precision, corresponding to one Cookie. This equivalence ratio is simply derived as the square of the ratio of height precisions, and yields 1.7 or 3.5 depending on mask angle (number of grazing reflections), indicating that one Cookie is equivalent to about 1.7 or 3.5 conventional altimeters of 3-cm precision each. Alternatively, it can be interpreted that, precision-wise, a Cookie is equivalent to a conventional altimeter with 2.3 or 1.6-cm precision, depending on the mask angle taken. It is noted that this comparison is very much simplified as the spatial and temporal scales that each type of altimeter would sample are very different. It is only to show that the Cookie can achieve a comparable performance to a conventional altimeter, and even better. In general it is expected that the Cookie would lead to a lower representation error in assimilation studies because of its better spatial and temporal coverage [38].

Regarding radio-occultation, one Cookie provides some 1843 rising and setting occultations per day, to be compared against the 250 or 1000 of each satellite of the COSMIC or COSMIC-2 constellations. In addition, each Cookie can observe 1140 daily side-looking occultations. The larger capability of the Cookie to capture radio-occultation events over conventional missions is mostly thanks to its beamformer, whose gain remains high and constant over azimuth angle.

VI. CONCLUSION

A satellite concept (dubbed "Cookie") for GNSS remote sensing constellations has been presented. Its shape is that of a flat cylinder, typically with two solar wings, to maximize access to direct, refracted and reflected GNSS signals and utilization of the volume of the launcher fairing. The Cookie can be split in two assemblies for ease of development: platform and payload. The most prominent subsystems of the instrument are the up- and down-looking beamfomers, whose antennas are accommodated in the center of the Cookie, and the interferometric processor, which can provide a wide range of precise observables from any GNSS satellite, although other types of processing techniques could also be embarked. Differently to previous satellites, the Cookie is pointed along the nadir–zenith line, and its agile steerable beams allow performing radio-occultation as well as forward and backward reflectometry in almost any direction. Several Cookies can be placed in orbit with a single launch, an attractive feature to build up a GNSS remote sensing constellation in the future, capable of a wide range of scientific and operational applications. As an example a constellation of three Cookies has been simulated, and its performance assessed to first order, by comparison to more conventional concepts. The Cookie can potentially outperform a conventional altimeter and a conventional radio-occultation satellite. The key concepts on which the payload of the Cookie is based upon can be demonstrated through ESA's GEROS-ISS.

ANNEX I

Equation (17) is derived as follows. It is assumed that in one particular 20 km × 20 km cell, after 10 days, there are M_a nadir looking altimetry measurements $\{h_1, h_2, \ldots, h_{\mathrm{Ma}}\}$ with a precision of σ_a and M_b altimetric observations at grazing angles $\{h_{\mathrm{Ma}+1}, h_{\mathrm{Ma}+2}, \ldots, h_{\mathrm{Ma}+\mathrm{Mb}}\}$ with a precision of σ_b. Then a weighted estimation of the sea surface height for this cell is built up which gives each of the two sets of altimetric data a weight proportional to the noise of the other set. This way the weighted observations have the same variance

$$h = \frac{\sigma_b}{M_b\sigma_a + M_a\sigma_b}\sum_{1}^{M_a} h_i + \frac{\sigma_a}{M_b\sigma_a + M_a\sigma_b}\sum_{M_a+1}^{M_a+M_b} h_i. \tag{AI-1}$$

Assuming all h_{i} measurements uncorrelated, the variance of the 10-day SSH height estimation is given by

$$\sigma_h^2 = \left(\frac{\sigma_b}{M_b\sigma_a + M_a\sigma_b}\right)^2 M_a\sigma_a^2 + \left(\frac{\sigma_a}{M_b\sigma_a + M_a\sigma_b}\right)^2 M_b\sigma_b^2. \tag{AI-2}$$

Operating yields

$$\sigma_h^2 = \left(\frac{\sigma_a\sigma_b}{M_b\sigma_a + M_a\sigma_b}\right)^2 (M_a + M_b) \tag{AI-3}$$

or

$$\sigma_h^2 = \left(\frac{M_b\sigma_a + M_a\sigma_b}{\sigma_a\sigma_b}\right)^{-2} (M_a + M_b). \tag{AI-4}$$

From this expression it is easy to derive (17)

$$\sigma_h = \sqrt{M_a + M_b}\left(\frac{M_a}{\sigma_a} + \frac{M_b}{\sigma_b}\right)^{-1}. \tag{AI-5}$$

ACKNOWLEDGMENT

The authors would like to thank the contribution of B. Martín-Barbera for producing an artist view and a 3-Dprinter model of the Cookie.

REFERENCES

[1] T. P. Yunck and G. F. Lindal, "The role of GPS in precise Earth observation," in *Proc. IEEE Position Location Navig. Symp.*, Nov. 29–Dec. 2, 1988, pp. 251–258.

[2] T. P. Yunck, C.H Liu, and R. Ware, "A history of GPS sounding," *Terr. Atmos. Ocean Sci.*, vol. 11, no. 1, pp. 1–20, 2000.

[3] G. Fjeldbo, "Bistatic-radar methods for studying planetary ionospheres and surfaces," Stanford Electronics Lab., Stanford, CA, USA, Sci. Report. no.2, NsG-377, SU-SEL-64-025, 1964.

[4] Mariner Stanford Group, "Venus: Ionosphere and atmosphere as measured by dual-frequency radio occultation of Mariner 5," *Science*, vol. 158, pp. 1678–1683, 1967.

[5] M. Martín-Neira, "A passive reflectometry and interferometry system (PARIS): Application to ocean altimetry," *ESA J.*, vol. 17, pp. 331–335, 1993.

[6] S. T. Lowe, J. L. LaBrecque, C. Zuffada, L. J. Romans, L. Young, and G. A. Hajj, "First spaceborne observation of an earth-reflected GPS signal," *Radio Sci.*, vol. 37, no. 1, Feb. 2002a.

[7] E. Cardellach, F. Fabra, O. Nogués-Correig, S. Oliveras, S. Ribó, and A. Rius, "GNSS-R ground-based and airborne campaigns for ocean, land, ice and snow techniques: Application to the GOLD-RTR datasets," *Radio Sci.*, vol. 46, Oct. 2011, Art. no. RS0C04.

[8] T. Elfouhaily, B. Chapron, and K. Katsaros, "A unified directional spectrum for long and short wind-driven waves," *J. Geophys. Res., Oceans*, vol. 102 , no. C7, pp. 15781–15796, Jul. 15, 1997.

[9] J. L. Garrison, S. G. Katzberg, and M. I. Hill, "Effect of sea roughness on bistatically scattered range coded signals from the global positioning system," *Geophys. Res. Lett.*, vol. 25, no. 13, pp. 2257–2260, Jul. 1, 1998.

[10] A. Komjathy, J. Maslanik, V. Zavorotny, P. Axelrad, S. J. Katzberg, "Sea ice remote sensing using surface reflected GPS signals," presented at the IEEE Int. Geoscience Remote Sensing Symp., Honolulu, HI, USA, Jul. 24–28, 2000.

[11] M. Belmonte, "Bistatic scattering of global positioning system signals from arctic sea ice," Ph.D. dissertation, Univ. Colorado, Boulder, CO, USA, 2007.

[12] F. Fabra, "GNSS-R as a source of opportunity for remote sensing of the cryosphere," Ph.D. dissertation, Inst. Space Stud. Catalonia, Catalonia, Barcelona, 2013.

[13] D. Masters, "Surface remote sensing applications of GNSS bistatic radar: Soil moisture and aircraft altimetry," Ph.D. dissertation, Univ. Colorado, Boulder, CO, USA, 2004.

[14] S. Paloscia *et al.*, "GNSS-R sensor sensitivity to soil moisture and vegetation biomass and comparison with SAR data performance," *Proc. SPIE*, vol. 8891, 2013, Art. no. 88910I.

[15] G.A. Hajj *et al.*, "Initial results of GPS–LEO occultation measurements of Earth's atmosphere obtained with the GPS/MET experiment," in *Proc. IAG Symp., G1, GPS Trends Precise Terr., Airborne, Spaceborne Appl., IUGG XXI Gen. Assembly*, Boulder, CO, USA, 1995.

[16] J. Wickert *et al.*, "GPS radio occultation with CHAMP: First results and status of the experiment," presented at the IAG Science Assembly, Vistas Geodesy New Millenium, Budapest, Hungary, 2001.

[17] G. Hajj *et al.*, "CHAMP and SAC-C atmospheric occultation results and intercomparisons," *J. Geophys. Res., Atmos.*, vol. 109, 2002, Art. no. 6109.

[18] J. Wickert *et al.*, "GPS radio occultation with CHAMP and GRACE: A first look at a new and promising satellite configuration for global atmospheric sounding," *Ann. Geophys.*, vol. 23, pp. 653–658, 2005.

[19] K. Cook, C. J. Fong, M. J. Wenkel, P. Wilczynski, N. Yen, and G. S. Chang, "FORMOSAT-7/COSMIC-2 GNSS radio occultation constellation mission for global weather monitoring," in *Proc. IEEE Aerosp. Conf.*, pp. 1–8, 2013.

[20] G. Beyerle and K. Hocke, "Observation and simulation of direct and reflected GPS signals in radio occultation experiments," *Geophys. Res. Lett.*, vol. 28, no. 9, pp. 1895–1898, May 1, 2001.

[21] S. Gleason *et al.*, Detection and processing of bistatically reflected gps signals from low Earth orbit for the purpose of ocean remote sensing," *IEEE Trans. Geosci. Remote Sens.*, vol. 43, no. 6, pp. 1229–1241, Jun. 2005.

[22] M. Unwin, S. Duncan, P. Jales, P. Blunt, and M. Brenchley, "Implementing GNSS-reflectometry in space on the TechDemoSat-1 Mission," presented at the ION GNSS+Conf., Tampa, FL, USA, Sep. 2014.

[23] C. Ruf, "The NASA EV-2 cyclone global navigation satellite system (CYGNSS) mission," presented at the JPL Sci. Visitor Colloq.—Earth Sci. Semin., Pasadena, CA, USA, vol. 27, Aug. 2012.

[24] M. Martín-Neira, S. D'Addio, C. Buck, N. Floury, and R. Prieto-Cerdeira, "The PARIS ocean altimeter in-orbit demonstrator," *IEEE Trans. Geosci. Remote Sens.*, vol. 49, no. 6, pp. 2209–2237, Jun. 2011.

[25] J. Wickert *et al.*, "GNSS REflectometry, Radio Occultation and Scatterometry onboard the International Space Station (GEROS-ISS)," presented at the ESA Living Planet Symp., Edinburgh, U.K., Sep. 13, 2013.

[26] T. P. Yunck, G. A. Hajj, E. R. Kursinski, J. A. LaBrecque, S. T. Lowe, and M. M. Watkins, "AMORE: An autonomous constellation concept for atmospheric and ocean observation," *Acta Astronaut.*, vol. 46, no. 2–6, pp. 355–364, 2000.

[27] A. Helm, G. Beyerle, R. Stosius, O. Montenbruck, S. Yudanov, and M. Rothacher, "The GNSS occultation, reflectometry, and scatterometry space receiver Gors: Current status and future plans within Gitews, presented at the 1st Colloquium of Scientific and Fundamental Aspects of the Galileo Programme, Cité de l'Espace, Toulouse, France, 2007.

[28] T. Meehan *et al.*, "Development status of NASA's TriG GNSS science instrument," presented at the IROWG-2 Workshop, Estes Park, CO, USA, 28th March–3rd April 2012.

[29] A. Rius *et al.*, "Altimetry with GNSSR interferometry: First proof of concept experiment," *GPS Solutions*, vol. 16, no. 2, pp. 231–241, Apr. 2012.

[30] E. Cardellach *et al.*, "Consolidating the precision of interferometric GNSS-R ocean altimetry using airborne experimental data," *IEEE Trans. Geosci. Remote Sens.*, vol. 52, no. 8, pp. 4992–5004, Aug. 2014.

[31] M. Martín-Neira, J. Hatton, M. Kern, J. Roselló, S. D'Addio, N. Floury, "System requirements for the GEROS-ISS payload," presented at the IEEE Int. Geoscience Remote Sensing Symp., QC, Canada, July 17, 2014.

[32] M. Martín-Neira, "GNSS interferometric radio occultation," *IEEE Trans. Geosci. Remote Sens.*, to be published.

[33] E. Cardellach *et al.*, "Sensitivity of PAZ LEO polarimetric GNSS radio-occultation experiment to precipitation events," *IEEE Trans. Geosci. Remote Sens.*, vol. 53, no. 1, pp. 190–206, Jan. 2014. doi:10.1109/TGRS.2014.2320309.

[34] S. T. Lowe, T. Meehan, and L. Young, "Direct-signal enhanced semi-codeless processing of GNSS surface-reflected signals," *IEEE J. Sel. Topics Appl. Earth Obs. Remote Sens.*, vol. 7, no. 5, pp. 1469–1472, May 2014.

[35] W. Li, D. Yang, S. D'Addio, and M. Martín-Neira, "Partial interferometric processing of reflected GNSS signals for ocean altimetry," *IEEE Geosci. Remote Sens. Lett.*, vol. 11, no. 9, pp. 1509–1513, Sep. 2014.

[36] P. Piironen, "PMS offset determination using an IF attenuator," ESA/ESTEC, Holland, The Netherlands, Tech. Note 14629/00/NL/SF, Jun. 2002.

[37] M. Martín-Neira *et al.*, "PARIS in-orbit demonstration mission: First end-to-end breadboard test results," pesented at the URSI Microwave Signatures, Special Symp. Microwave Remote Sensing Earth, Moon, Atmosphere, Espoo, Helsinki, Finland, Oct. 28–31, 2013.

[38] P. R. Oke and P. Sakov, "Representation error of oceanic observations for data assimilation," *J. Atmos. Ocean. Technol.*, vol. 25, pp. 1004–1017, Jun. 2008.

[39] J. Wickert *et al.*, "GNSS reflectometry with GEROS-ISS: Overview and recent results," presented at the IEEE Int. Geoscience Remote Sensing Symp., Milan, Italy, 2015.

[40] A. Camps, H. Park, A. Ghavidel, J. M. Rius, and I. Sekulic, "GEROS-ISS: A demonstration mission of GNSS remote sensing capabilities to derive geophysical parameters of the Earth surfaces: Altimetry performance evaluation," presented at the IEEE Int. Geoscience Remote Sensing Symp., Milan, Italy, 2015.

Manuel Martín-Neira (SM'96) received the M.S. and Ph.D. degrees in telecommunication engineering from the School of Telecommunication Engineering, Polytechnic University of Catalonia, Spain, in 1986 and 1996 respectively.

He received fellowship to work on radiometry at European Space Research and Technology Center, Noordwijk, The Netherlands, in 1988. From 1989 to 1992, he joined GMV, a Spanish firm, where he was responsible for several projects for the European Space Agency (ESA) related to GPS spacecraft navigation with applications to precise landing and attitude determination. Since 1992, he has been the In-Charge of the radiometer activities within the Payload, Equipment and Technology Section, ESA. During this period, he has also developed new concepts for constellations of small satellites for Earth observation. In particular, he holds a patent on the PARIS concept for the use of GNSS signals reflected from the ocean.

Dr. Martín-Neira received the Confirmed Inventor Award from the director of ESA in 2002 and is a Member of the Academie des Technologies of France since 2009. He is currently the Instrument Principal Engineer of ESA's Soil Moisture and Ocean Salinity Earth Explorer Opportunity Mission.

Weiqiang Li received the B.S. degree in electronic engineering and the Ph.D. degree in communication and information system from BeiHang University, Beijing, China, in 2004 and 2012, respectively. His Ph.D. dissertation was on the signal processing methods and instrumentation of the earth reflected GNSS signal for remote sensing purposes.

He is currently a Postdoctoral Research Fellow at the Earth Observation Research Group, Institute of Space Sciences, Barcelona, from 2014, working in the definition of a small satellite constellation for GNSS remote sensing.

Ana Andrés-Beivide received the M.S. degree in telecommunications engineering from the University of Cantabria, Cantabria, Spain, in 2005.

From 2006 to 2008, she joined the Radio Frequency Payload Systems Division, European Space Research and Technology Center, Noordwijk, The Netherlands, first as Spanish Trainee and later as a Contractor, focusing her work on the research, design, development, and test of microwave active devices and on the analysis of RF active chains. Since 2009, she has been working at Airbus Defence & Space (former EADS Casa Espacio), Madrid, Spain, on the design and test of RF payloads for Earth observation and navigation. She has been involved in the development of different families of instruments, mainly active and passive remote sensors. Her technical interests include the research of new concepts and architectures for microwave instruments.

Xabier Ballesteros-Sels received the M.S. degree in telecommunication engineering from the School of Telecommunication Engineering, Polytechnic University of Catalonia, Spain, in 2006.

He was awarded a fellowship to carry out the M.S. thesis at the Department of Photonics Engineering, Technical University of Denmark, where he worked on adaptive compensation of optical transmission impairments by means of electrical equalization. In 2007, he joined the Space and Microwave Division of Mier Comunicaciones, a Spanish company devoted to the design and manufacturing of advanced space qualified microwave equipment and subsystems. He works as an RF Design Engineer and Technical Manager (project technical responsible), focusing his activities in L/S-band ultra-low noise amplifier units and receivers, and also in multiple inputs/outputs standalone power dividers, hybrids, and couplers for SATCOM payloads. In addition to this, he has been involved in several Phase A studies such as the PARIS concept, from the feasibility study to the breadboard of some critical RF parts of the system.